considerations. In particular, the hole may be shared equally by the six nearest-neighbor oxygen ions which would, of course, exhibit cubic symmetry. To account for the observed axial symmetry, one may invoke a Jahn-Teller-type distortion. In any event, it is apparent that the V^-, [Li]^0, and [Na]^0 defect centers are obviously similar in nature in MgO, CaO, and SrO, and presumably the correct model would have to account for the properties of this entire class of defect centers.

†Research sponsored by the U. S. Atomic Energy Commission under contract with Union Carbide Corp.

*Deceased.

‡Guest Scientist from University of Alabama, Birmingham, Ala.

[1]J. E. Wertz, P. Auzins, J. H. E. Griffiths, and J. W. Orton, Discussions Faraday Soc. 28, 136 (1959).

[2]A. J. Shuskus, J. Chem. Phys. 39, 849 (1963).

[3]J. L. Kolopus, Ph.D. thesis (University of Missouri, Columbia, 1965) (unpublished); J. T. Suss, Ph.D. thesis (Hebrew University, Jerusalem, 1966) (unpublished).

[4]J. E. Wertz, G. S. Saville, P. Auzins, and J. W. Orton, J. Phys. Soc. Japan Suppl. 18, 305 (1963).

[5]Y. Chen and W. A. Sibley, Phys. Rev. 154, 842 (1967).

[6]O. F. Schirmer, J. Phys. Chem. Solids 32, 499 (1971).

[7]H. T. Tohver, B. Henderson, Y. Chen, and M. M. Abraham, Phys. Rev. B (to be published).

[8]W. A. Sibley, J. L. Kolopus, and W. C. Mallard, Phys. Status Solidi 31, 223 (1969).

[9]M. M. Abraham, C. T. Butler, and Y. Chen, J. Chem. Phys. 55, 3752 (1971).

[10]W. E. Hagston, J. Phys. C 3, 1233 (1970).

[11]A. E. Hughes and B. Henderson, in *Defects in Crystalline Solids*, edited by J. H. Crawford, Jr., and L. M. Slifkin (Plenum, New York, 1971), and references therein.

PHYSICAL REVIEW B VOLUME 5, NUMBER 12 15 JUNE 1972

Lattice Dynamics of Pyrolytic Graphite*

R. Nicklow, N. Wakabayashi, and H. G. Smith

Solid State Division, Oak Ridge National Laboratory, Oak Ridge, Tennessee 37830

(Received 3 December 1971)

The frequencies of certain normal modes of vibration of the graphite lattice have been studied on samples of high-quality pyrolytic graphite by coherent, inelastic-neutron-scattering techniques. Some of the data are not compatible with certain restrictions imposed by the valence-bond model as presented by Young and Koppel. Therefore, the data have been analyzed in terms of a simple axially symmetric, Born–von Kármán force-constant model. The results show that appreciable interactions exist between third nearest neighbors in the basal plane. The force model has been used to calculate a frequency distribution function and the lattice specific heat of graphite. These calculations are in excellent agreement with the specific heat measured for natural graphite in the temperature range 1.5–300 °K.

I. INTRODUCTION

It is well known that the forces between the atoms in graphite are extremely anisotropic[1–4]; those between adjacent basal planes are about two orders of magnitude smaller than the forces between neighboring atoms in the same plane, which are comparable to the exceptionally strong interatomic forces existing in diamond. In fact these interplanar forces are so weak that it is necessary to handle a crystalline graphite sample carefully in order to avoid cracking it or cleaving flakes from its (001) faces. Consequently, the vibrational modes, which correspond to the displacements of atoms relative to others on the same basal plane, have very high frequencies, whereas modes in which the basal planes move essentially as rigid units have quite low frequencies.

These lower-frequency modes were studied with neutron-coherent-inelastic-scattering techniques by Dolling and Brockhouse.[5] The major difficulty of any such study on graphite is the lack of large single-crystal samples. At present only pyrolytic graphite samples consisting of very thin (~1 μ) graphite crystallites randomly oriented about a common c axis are available. Thus, as discussed by Dolling and Brockhouse,[5] essentially the only portion of the phonon dispersion relation that can be studied unambiguously by coherent-neutron-scattering measurements is that corresponding to the longitudinal modes propagating along the [001] direction. However, they were able to obtain limited information about the lowest-frequency transverse modes propagating along the same direction.

Since the time of this earlier work the quality of pyrolytic graphite has improved considerably. It is

now possible to obtain large samples having ~0.4° angular spread of the c axis, compared to the ~5° spread of the samples used previously. Thus we considered it desirable to investigate the possibility of extending the work of Dolling and Brockhouse. In particular as a result of a study of the lattice dynamics of several hexagonal metals[6,7] it became apparent to us that vibrational modes, having wave vectors in but polarization vectors normal to the basal plane (the $TA_\perp$ and $TO_\perp$ modes), can be very isotropic at small wave vectors. If this isotropy also exists in graphite, a rotation about the c axis, thereby simulating the effects of the orientation randomness of pyrolytic graphite, merely moves the dispersion surface for these modes parallel to itself. Since the neutron-scattering geometry generally used to study these modes uniquely defines $|\vec{q}|$, the magnitude of the wave vector, a measurement of frequency vs $|\vec{q}|$ could be carried out to determine the shape of this dispersion surface for small $|\vec{q}|$. It was hoped that such a measurement could yield the first direct information about the range of the interatomic forces in the basal plane. Actually it has been possible to measure well-defined neutron groups for wave vectors with magnitudes corresponding to the Brillouin-zone boundary in the [100] direction, i.e., the M point. In addition it has been possible to obtain limited information about the longitudinal modes propagating in the basal plane.

II. EXPERIMENTS

The measurements were performed with a triple-axis neutron spectrometer located at the Oak Ridge High Flux Isotope Reactor. The (002) planes of Be crystals were used as monochromator and analyzer and Soller slits (40′ horizontal angular resolution) were placed before and after the sample. The sample crystal was oriented with the c axis in the plane of scattering. Four different scattering configurations were used in the measurements, three of which are shown schematically in Fig. 1. The reciprocal lattice of pyrolytic graphite consists of the reciprocal lattice of the ideal graphite structure, rotated about the [001] direction (the c axis) to produce smeared-out "rings" of reciprocal-lattice points except along the [001] direction itself. The rings shown in Fig. 1 represent the 110- and 100-type reciprocal-lattice points after such a rotation. The scattering plane contains the c axis, the incident neutron wave vector $\vec{k}_0$, and the scattered neutron wave vector $\vec{k}'$.

For configuration I, constant-$\vec{Q}$ measurements were carried out with the scattered neutron energy E' fixed at approximately 6 THz. In this configuration the frequencies of the longitudinal modes propagating along the c direction can be measured unambiguously as a function of wave vector. The results obtained for the acoustic modes LA and the lowest-frequency optic modes LO are shown in Fig. 6. The present measurements give frequencies which are slightly lower than those obtained previously.[5] This difference is undoubtedly due to the larger mosaic spread of the sample used in the earlier work which gave rise to contributions to the observed neutron groups from the higher-frequency modes that have wave vectors slightly off the [001] direction.

With configuration II, constant-$\vec{Q}$ measurements were carried out, also with E' fixed at 6 THz, to determine the frequencies of the transverse acoustic modes and the lowest-frequency optic modes propagating along the [001] direction. Hereafter these will be called the $TA(0,0,\zeta)$ and $TO(0,0,\zeta)$ modes. As indicated by the dashed arrows in Fig. 1, the wave-vector component perpendicular to the scattering plane is not well defined in this experiment because any point on the 110 ring is an origin for a wave vector. In addition, the finite q resolution of the instrument permits the observation of scattering by phonons with wave vectors in the scattering plane but which are also inclined to the [001] direction. However, one expects the frequencies of the transverse $(0,0,\zeta)$ modes to be lower than those of all other modes observable in this configuration, since these other modes involve a distortion of the very stiff basal plane. It should be pointed out that the structure factors for the $TA(0,0,\zeta)$ and $TO(0,0,\zeta)$ modes alternate between 0 and 1 in successive Brillouin zones along c, such that only one of the branches is visible in a given zone. Thus as the frequency is scanned in a constant-$\vec{Q}$ experiment one should observe no phonon scattering below $\nu_T(\zeta)$, the frequency corresponding to the visible

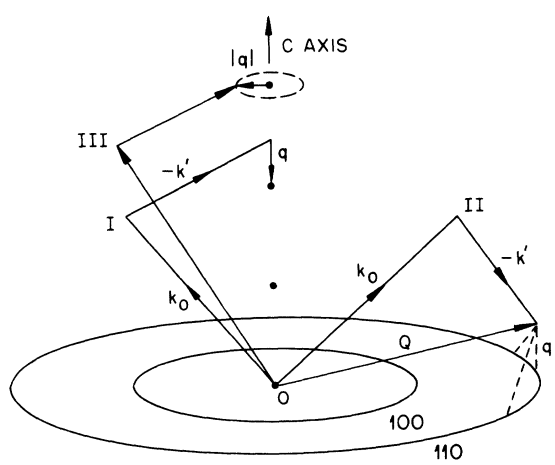

FIG. 1. Reciprocal-space diagram for pyrolytic graphite showing three of the neutron-scattering configurations used in the present work.

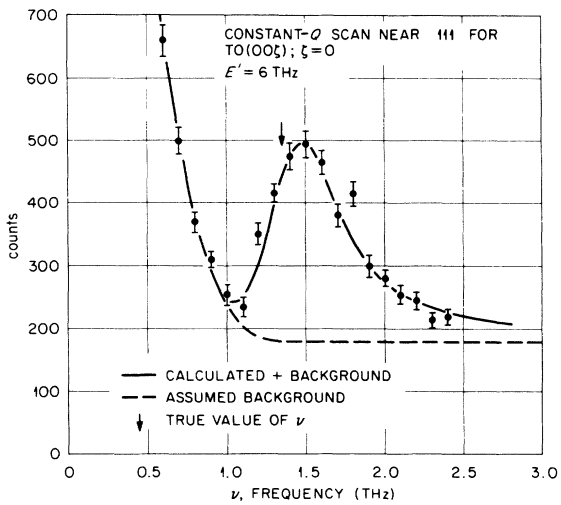

FIG. 2. Comparison of a calculated and measured constant-Q scan of the TO(00ζ) branch for $\zeta = 0$.

transverse mode with the wave vector $\vec{q} = (0, 0, \zeta) \times 2\pi/c$. Then as $\nu_T(\zeta)$ is reached in the scan, a rapid increase in the scattering is expected. Above $\nu_T(\zeta)$ the scattering by phonons having wave vectors inclined to the [001] direction dominates. However, the intensity of this scattering will decrease (slowly) with increasing ν, primarily because of the frequency-dependent factors in the neutron-scattering cross section, viz.,

$$(1/\nu)[1 + (e^{h\nu/kT} - 1)^{-1}],$$

although the polarizations of the phonons involved and the magnitude of the instrumental q resolution in the scattering plane also are important. The net result is that the maximum of the intensity distribution of neutrons obtained in a configuration-II experiment always occurs at a frequency which is slightly higher than $\nu_T(\zeta)$.

A detailed numerical calculation of the intensity distribution expected for TO(0, 0, ζ) at $\zeta = 0$ has been carried out and is described in the Appendix. The result of this calculation is compared to the experimental data in Fig. 2. The background level assumed in the comparison (the dotted line in Fig. 2) is dictated by some general qualitative results, obtained from several such calculations, concerning the amount of true one-phonon scattering expected at frequencies well above $\nu_T(\zeta)$. At present the source of the increasing background level below 1.0 THz is not known. The general shapes of several calculated intensity distributions were rather insensitive to the value chosen for ν_T, although obviously the peak positions varied with ν_T. The value used in the calculation illustrated in Fig. 2 is 1.35 THz.

On the basis of the excellent agreement obtained between the calculated and experimental results as shown in Fig. 2, we conclude that the important contributions to the measured scan have been correctly taken into account in the calculation, and that the true frequency of the TO phonon with zero wave vector is very nearly 1.35 THz. This frequency, indicated by the arrow in the figure, corresponds to an intensity which is about 80% of the maximum (above the assumed background) observed near 1.48 THz. Although we have not carried out calculations for other values of ζ (for which small changes in the details of our calculation for $\zeta = 0$ may be required), the similarity between the shapes of the experimental results for different ζ along the transverse (0, 0, ζ) branch, and the insensitivity to variations in ν_T of the calculated shapes for $\zeta = 0$, suggest that a reasonable value for the true frequency at each ζ is that appropriate to an intensity which is approximately 80% of the maximum observed in each scan. The (uncorrected) frequencies corresponding to the positions of the intensity maxima are plotted in Fig. 6.

In configuration III most of the measurements were performed using the constant-energy method with E' fixed at 6 THz, although for small $|\vec{q}|$ and for $|\vec{q}| = 0.5(4\pi/\sqrt{3}a)$ constant-$\vec{Q}$ measurements were made. Neutron-scattering results near all the lattice points 002 to the 007 were studied. It is in this configuration that the transverse modes, having wave vectors in and polarizations perpendicular to the basal plane, were investigated. As was mentioned above, well-defined neutron groups are expected for small $|\vec{q}|$. However, even at rather large $|\vec{q}|$ well-defined, though broadened, groups were observed as indicated in Fig. 3(a) where a constant-energy scan is shown, and in Fig. 3(b) where a constant-$\vec{Q}$ scan for $|\vec{q}| = 0.5(4\pi/\sqrt{3}a)$ is shown. This latter scan corresponds to a wave-vector magnitude equal to that appropriate for the Brillouin-zone boundary in the [100] direction, i.e., the M point. It is worth mentioning that constant-$\vec{Q}$ scans were carried out at the M point because the dispersion surfaces at that point for both the acoustic and optic modes have horizontal tangents.

The general picture that emerges from the data obtained in configuration III is close to that anticipated. That is, at low $|\vec{q}|$, e.g., $\leq 0.2(4\pi/\sqrt{3}a)$, the $TA_\perp$ and $TO_\perp$ dispersion surfaces are very isotropic so that the widths of the measured neutron groups were mainly due to the instrumental resolution. As $|\vec{q}|$ increases the observed peak width increases, indicating a small departure from perfect isotropy. In this case a high-resolution constant-$\vec{Q}$ scan would measure the distribution of frequencies for those $TA_\perp$ (or $TO_\perp$) modes which all have the same $|\vec{q}|$. In the early phases of this work we carried out calculations of such distribution functions, using several preliminary force models and a modification of the frequency-distribution

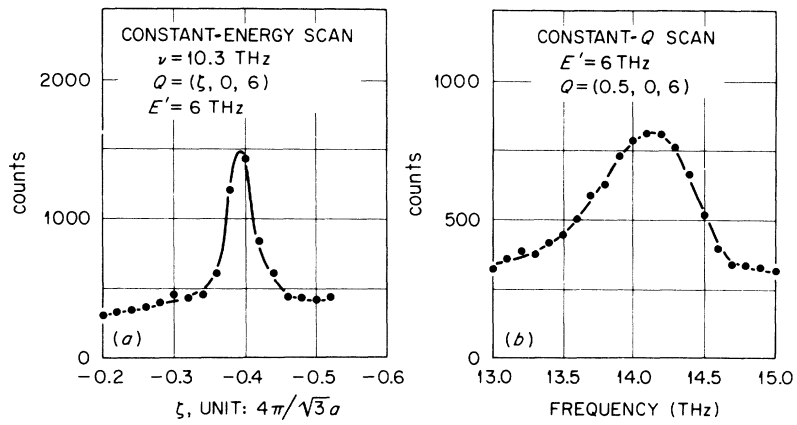

FIG. 3. (a) Typical constant-energy scan obtained for $TA_\perp$ branch at high ζ. (b) Constant-Q scan for $TA_\perp$ branch for $|\vec{q}|$ appropriate to (100) zone boundary.

calculation method outlined by Raubenheimer and Gilat,[8] in order to investigate the shapes to be expected for them. One result which is typical of those obtained is shown in Fig. 4. Most of the scans actually obtained in configuration III near the $|\vec{q}|$ shown in Fig. 4 were constant-energy scans. Nevertheless, the calculations did at least indicate that the distribution of frequencies between the extreme values, corresponding here to wave vectors along [100] and [110] directions, was reasonably uniform. When smeared out by the instrumental resolution, such a frequency distribution may be expected to give rise to a neutron group whose peak position would be intermediate between the values of these extreme frequencies and whose width would be proportional to the departure from isotropy of the dispersion surface.

As $|\vec{q}|$ is increased the neutron groups continue to be rather well defined up to $|\vec{q}| \simeq 0.5(4\pi/\sqrt{3}a)$. Any $|\vec{q}|$ larger than this value is beyond the Brillouin-zone boundary and the dispersion curves for $\vec{q}$ along the [100] and [110] directions are no longer nearly superimposed. In fact, no easily interpretable neutron groups were obtained for $|\vec{q}| > 0.5(4\pi/\sqrt{3}a)$. The results of the measurements in configuration III are shown in Fig. 6 by open circles for $|\vec{q}| \leq 0.2(4\pi/\sqrt{3}a)$ and by bars, representing the widths at half-intensity of the neutron groups observed, for $0.2(4\pi/\sqrt{3}a) < |\vec{q}| \leq 0.5(4\pi/\sqrt{3}a)$.

Configuration IV is similar to II except that $\vec{Q}$ (and $\vec{q}$) is in the basal plane. In this configuration constant-energy scans were carried out with E' fixed at 6 or 3.3 THz to study the LA and lowest-frequency LO modes having wave vectors in the basal plane. For reasons already mentioned above for configuration II, the phonon wave vector is not well defined in configuration IV. However, similar to observations for configuration II, there are ranges for ν and $\vec{q}$ where no phonon scattering is expected. For example, at a point $\vec{Q} = (1+\zeta,\ 1+\zeta,\ 0)4\pi/\sqrt{3}a$, just beyond the 110 ring, the shortest wave vector of a phonon that can contribute to the scattering is $(\zeta, \zeta, 0)4\pi/\sqrt{3}a$. Any other wave vector connecting this $\vec{Q}$ with a point on the 110 ring is longer, and therefore belongs to a phonon having a frequency higher than that with the wave vector $(\zeta, \zeta, 0)4\pi/\sqrt{3}a$. If the energy transfer of the neutron $(E_0 - E')/h = \nu$ is chosen so that the frequency ν is smaller than $\nu_L(\zeta)$, the frequency of the longitudinal (110) branch at ζ, no scattering will be observed. Then as ζ is reduced, as in a constant-energy scan, a rapid increase in the neutron-scattering intensity will occur

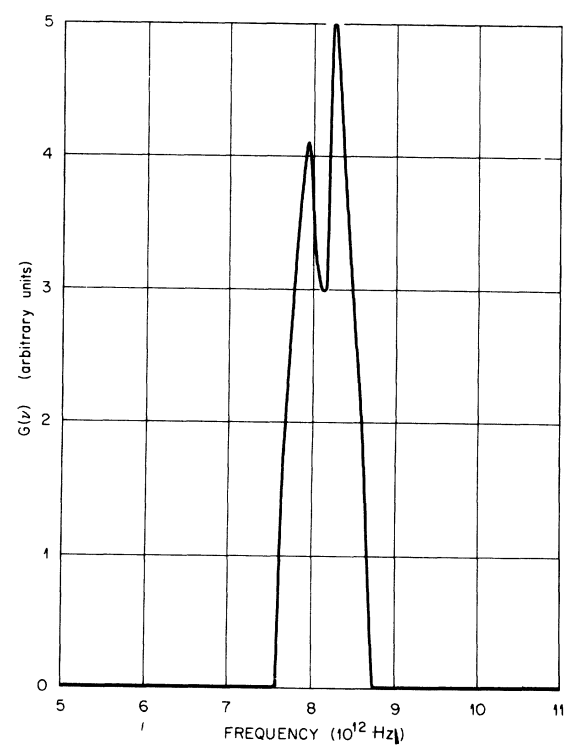

FIG. 4. Calculated frequency distribution for $TA_\perp$ branch for $|\vec{q}| = 0.35(4\pi\sqrt{3}a)$.

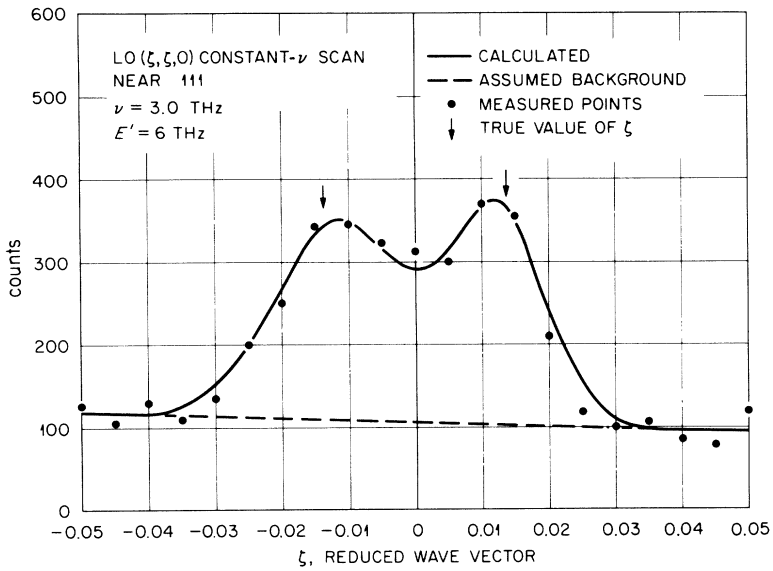

FIG. 5. Comparison of a calculated and measured constant-ν scan of the LO ($\zeta\zeta 0$) branch for $\nu = 3.0$ THz.

when ζ reaches a value so that $\nu = \nu_L(\zeta)$. For still smaller ζ the intensity may remain high, even though ν will then be greater than $\nu_L(\zeta)$, because of the scattering from longitudinal and transverse modes with wave vectors out of the scattering plane. The intensity will then drop abruptly inside the 110 ring for $\vec{Q} = (1-\zeta,\ 1-\zeta,\ 0)4\pi/\sqrt{3}a$ when again $\nu < \nu_L(\zeta)$.

Numerical calculations of the scattering expected for such constant-energy scans are also described in the Appendix. The results of a calculation carried out for the $(\zeta, \zeta, 0)$ LO mode which is degenerate with the TO $(0, 0, \zeta)$ branch at $\zeta = 0$ are compared to the experimental results in Fig. 5. The calculated intensity distribution when added to a slightly sloping background is in excellent agreement with the experimental results. The intensity of the calculated curve was scaled to reproduce approximately the maximum experimental intensity. One common and expected feature of all such calculations is the small shift of the peak position toward values of ζ smaller than those which correspond to the true values defined by $\nu = \nu_L(\zeta)$. The corrected experimental results obtained for the longitudinal branches are shown in Fig. 6, where ζ is expressed in units appropriate for the [100] direction. Data were obtained near the 110, 111, and 100 rings. Well-defined peaks were observed at low frequency, but the intensity decreased so rapidly with increasing frequency that reliable data could not be obtained above ~12 THz.

III. THEORETICAL CALCULATIONS

A. Force Models and Data Analysis

A perspective illustration which shows the positions of the atoms in graphite is given in Fig. 7. The atoms labeled A, B, C, and D are all in the same primitive unit cell. Atoms B, E (and E′), F, and C are, respectively, the first, second, third, and fourth nearest neighbors of A. In the present work we have limited our consideration to force models which include interactions extending to the fourth-nearest-neighbor atoms. This is a natural limitation because the shortest distance between adjacent basal planes (i.e., between A and C) corresponds to the fourth-nearest-neighbor distance, and it is certainly desirable to include this interaction in any force model of graphite. On the other hand, with the small amount of data available, consideration of additional interactions between more distant neighbors either in the same basal plane or in adjacent planes would be fruitless. We also have not considered models which allow for the possible existence of long-range electrostatic forces or of the polarizability of atoms as has been used in the shell models applied to diamond.[9]

The force-constant matrices of a general tensor force model for graphite are given in Table I. Actually this model is not rigorously complete because the symmetry of the graphite lattice would allow certain second-neighbor force constants to be different, e.g., those between B-B′ can be different from those between A-E′. However, if we could ignore the influence of the adjacent planes on the interactions within a plane, these two sets of force constants could be assumed to be identical. In any event, even with this assumption there are 12 independent force constants in the model and further approximations are desirable.

Two models which are special cases of a general tensor force model are commonly used: the bond-bending and bond-stretching model (BBS) and the

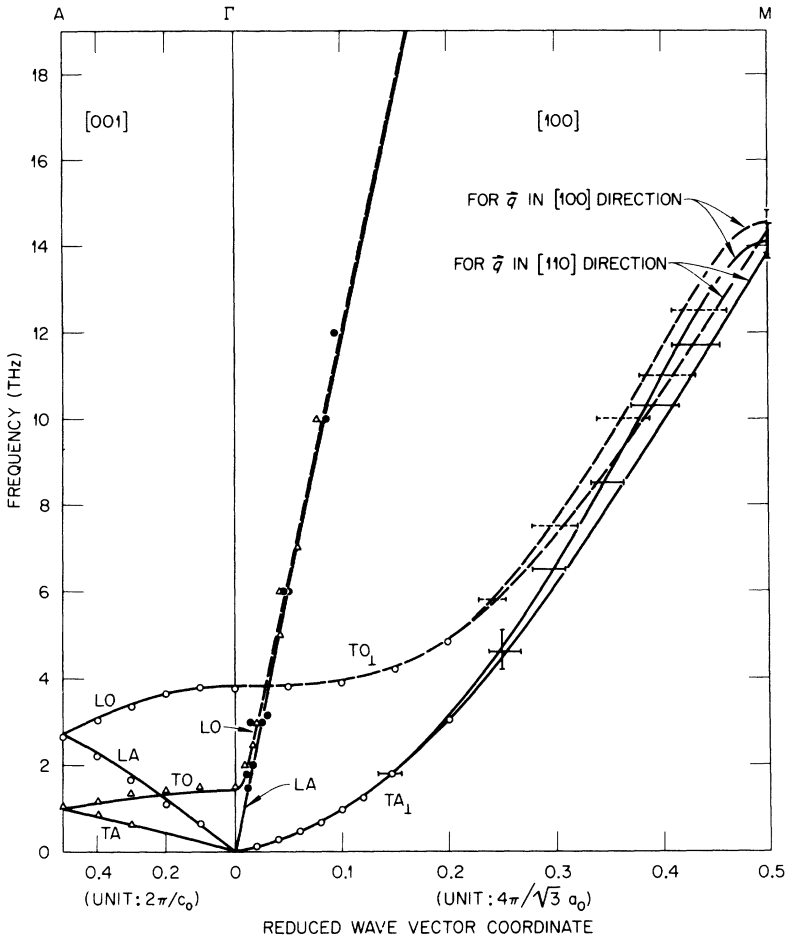

FIG. 6. Phonon frequencies measured for pyrolytic graphite. All measurements for $\vec{q}$ in the basal plane have been plotted with $\vec{q}$ expressed in units appropriate for the [100] direction. The lines shown represent calculations with the fourth-nearest-neighbor AS model discussed in the text. For the $TA_\perp$ and $TO_\perp$ branches calculations for $\vec{q}$ in both the [100] and [110] directions are shown to illustrate the approximate isotropy of these branches.

axially symmetric model (AS). The details of the BBS model as applied to graphite have been described most recently by Young and Koppel.[4] Their model is equivalent to the following restrictions:

$$\alpha_1 = \kappa, \quad \beta_1 = 6\mu, \quad \gamma_1 = \tfrac{2}{3}\mu',$$

$$\alpha_2 = -\tfrac{3}{4}\mu, \quad \beta_2 = \tfrac{1}{4}\mu, \quad \gamma_2 = -\tfrac{1}{9}\mu', \quad \epsilon_2 = \tfrac{1}{4}\sqrt{3}\,\mu,$$

TABLE I. General force-constant matrices for graphite.

Neighbor relative to origin atom[a]	Coordinate of typical atom	Matrix elements ϕ_{xy}
first	B′: $(-a/\sqrt{3},\ 0,\ 0)$	$\alpha_1\ 0\ 0$ $0\ \beta_1\ 0$ $0\ 0\ \gamma_1$
second	E: $(0,\ a,\ 0)$	$\alpha_2\ \epsilon_2\ 0$ $-\epsilon_2\ \beta_2\ 0$ $0\ 0\ \gamma_2$
third	F: $(2a/\sqrt{3},\ 0,\ 0)$	$\alpha_3\ 0\ 0$ $0\ \beta_3\ 0$ $0\ 0\ \gamma_3$
fourth	C: $(0,\ 0,\ \frac{1}{2}c)$	$\alpha_4\ 0\ 0$ $0\ \alpha_4\ 0$ $0\ 0\ \gamma_4$

[a]Atom A in Fig. 7.

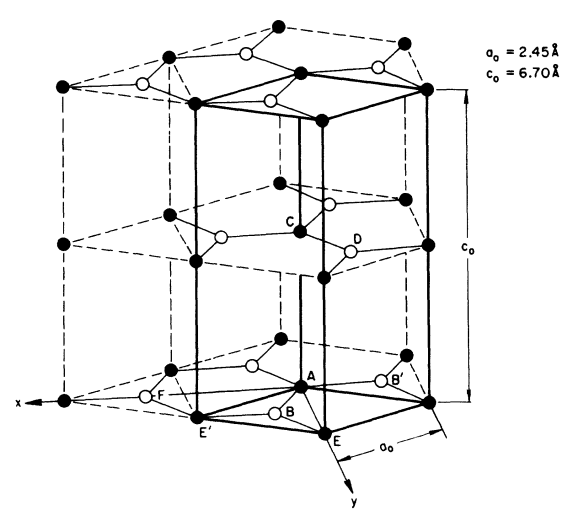

FIG. 7. Perspective drawing showing positions of the atoms in graphite.

$$\alpha_3=\beta_3=\gamma_3=0, \quad \alpha_4=0, \quad \gamma_4=\kappa'.$$

Here κ is the bond-stretching force constant between nearest neighbors such as A-B, μ is a bond-bending force constant which describes the force necessary to change the angle formed by the A-B and A-B′ bonds, μ' is a bond-bending force constant which describes the force necessary to displace an atom along the c axis relative to its nearest neighbors in the same plane, and κ' is a bond-stretching force constant between nearest neighbors on adjacent planes such as A-C. Note that for this model $\gamma_1 = -6\gamma_2$.

In the AS model it is assumed that there is a two-body potential function $V(r)$ which describes the forces between any pair of atoms and which depends only on the distance between the atoms. This assumption leads to the following restrictions:

$$\alpha_1=\phi_r^1, \quad \beta_1=\phi_t^1, \quad \gamma_1=\phi_t^1 \ ,$$
$$\alpha_2=\phi_t^2, \quad \beta_2=\phi_r^2, \quad \gamma_2=\phi_t^2 \ ,$$
$$\alpha_3=\phi_r^3, \quad \beta_3=\phi_t^3, \quad \gamma_3=\phi_t^3 \ ,$$
$$\alpha_4=\phi_t^4, \quad \gamma_4=\phi_r^4,$$

where

$$\phi_r^n=\left(\frac{\partial^2 V}{\partial r^2}\right)_{r=r_n}, \quad \phi_t^n=\left(\frac{1}{r}\frac{\partial V}{\partial r}\right)_{r=r_n},$$

and r_n is the distance between atoms which are the nth nearest neighbors of each other. In this model the force constants for the B-B′ and A-E′ interactions are necessarily identical.

The BBS model is more appealing on physical grounds because it appears to be a natural consequence of the concept of strong covalent bonding between carbon atoms. However, this model as previously formulated neglects the third-neighbor interactions while a part of the fourth-neighbor interaction is included. Also for this model the elastic constant $C_{44}=0$ because $\alpha_4=0$ and $\gamma_1=-6\gamma_2$. Including bond-stretching forces between more distant neighbors does not remedy this nonphysical property. Furthermore, early in this work it was found that the shapes of the $TA_\perp$ and $TO_\perp$ branches, which depend only on γ_1, γ_2, and γ_3, could not be satisfactorily reproduced with the restriction $\gamma_1 = -6\gamma_2$ even for $\gamma_3 \neq 0$. Thus the analysis of the data presented here has been carried out in terms of an AS model.

The AS model, while not as physically appealing as the BBS model, is a somewhat more general model for vibrations perpendicular to the basal plane since no relation between the γ_i's (hereafter ϕ_t^i) is imposed; also $\phi_t^4 \neq 0$ thereby giving a finite C_{44}. Actually the ϕ_t^i constants are not independent because the initial slope at $\vec{q} \to 0$ of the $TA_\perp$ branch, which depends only on ϕ_t^1, ϕ_t^2, and ϕ_t^3, and that of the $TA(00\zeta)$ branch, which depends only on ϕ_t^4, are both determined by C_{44}. Thus one finds for the AS (and the general tensor) model,

$$\phi_t^4=(\tfrac{1}{2}\phi_t^1+3\phi_t^2+2\phi_t^3)a^2/c^2. \tag{1}$$

The data obtained here can be naturally subdivided into small portions each of which relates rather directly to only a few of the force constants. Thus the analysis was carried out in several stages, and at each stage only those force constants which strongly influenced the portion of the data being analyzed were evaluated. First the constants ϕ_t^4 and ϕ_r^4 were determined from a least-squares analysis of the data obtained for the longitudinal and transverse branches along [001] that were studied in configurations I and II. Then, keeping these constants fixed, ϕ_t^1, ϕ_t^2, and ϕ_t^3 were determined from an analysis of the $TA_\perp$ and $TO_\perp$ branches with the restriction expressed in Eq. (1) included. In this part of the analysis we required the calculated dispersion curves to be isotropic within the widths of the neutron groups observed in configuration III.

Finally, the force constants ϕ_r^1, ϕ_r^2, and ϕ_r^3 were determined by a least-squares fitting of the longitudinal modes studied in configuration IV with all the other constants held fixed at the values determined by the methods mentioned above. However, since only very limited information for these modes was available in the neutron measurements, the value of the Raman frequency[10] (1575 cm^{-1}) and the value of the elastic constant C_{66} measured by Seldin[11] were included in this stage of the analysis. The lines in Fig. 6 show the fit to the neutron data obtained with this model.

The values obtained for all the force constants are given in Table II. The errors given in Table II are estimates which include experimental uncertainties and the variations in the parameters which were obtained when the procedures of the analyses were varied slightly from the procedure described above. The ϕ_r^1, ϕ_r^2, and ϕ_r^3 parameters are rather poorly determined by the sparse data presently available for the longitudinal modes in the basal plane. It is difficult to make a direct comparison of the values of these constants and those of the BBS model reported by Young and Koppel[4] since the two models are based on different general physical assumptions. About all that can be concluded generally is that those constants which describe similar atomic motions in the two models, i.e., that of one atom relative to another, have

TABLE II. Force constants for graphite (10^5 dyn/cm).

ϕ_r^1	3.62 (±25%)	ϕ_r^3	−0.037 (±100%)
ϕ_t^1	1.99 (±3%)	ϕ_t^3	0.288 (±3%)
ϕ_r^2	1.33 (±30%)	ϕ_r^4	0.058 (±2%)
ϕ_t^2	−0.520 (±3%)	ϕ_t^4	0.0077 (±5%)

similar orders of magnitude. Moreover, the restrictions of the BBS model, $6\phi_t^2 = -\phi_t^1$ and $\phi_t^3 = 0$, as mentioned above are not compatible with the results obtained here for the $TA_\perp$ and $TO_\perp$ branches. Indeed, the restriction imposed by Eq. (1) gives $6\phi_t^2 + 4\phi_t^3 \simeq -\phi_t^1$, since $\phi_t^4 \simeq 0$ (i.e., $\alpha_4 \simeq 0$) in comparison to the other constants in Eq. (1). Thus if $\phi_t^3 \simeq 0$, the restrictions of the two models on the z displacements would be very similar. The relatively large magnitude of ϕ_t^3 indicates that there is a significant force in the z direction on atom A when atom F is displaced in the z direction. In terms of a bonding picture the existence of such a force could perhaps be interpreted to mean that a bond such as E'-B possesses a considerable resistance to twisting.

B. Calculations from Model

A calculation of the entire dispersion relation for graphite in the [100], [110], and [001] directions is shown in Fig. 8. In the [100] and [110] directions there are 12 distinct frequencies for each wave vector. However, because of the very small magnitude of ϕ_t^4, modes corresponding to atomic displacements parallel to the basal planes are nearly degenerate in pairs except at low frequencies near Γ. Each line in Fig. 8 which goes to any one of the four highest frequencies at M represents such a pair.

Obviously the neutron measurements shown in Fig. 6 correspond to a very small portion of the frequency range encompassed by the normal modes in graphite. Thus the absolute accuracy of the derived force constants and, hence, of the calculated high-frequency branches is very difficult to assess. However, several seemingly reliable neutron groups were observed in our experiments on the $TO_\perp$ branch for $\nu \sim 17-30$ THz. The results were not used in the fitting analysis but nevertheless they are in fairly good agreement ($\sim 5\%$) with the calculated curves. Furthermore, the optical data, which were used in the fitting analysis, accurately pin down the location of the highest-frequency branch (LO) at Γ. On the other hand, the AS model was found to be inadequate when used in an analysis of a rather complete measurement[6] of the dispersion relation of the hexagonal metal Tb, and there is no reason to expect such a model to be more reliable for graphite. Thus, while the qualitative features of the high-frequency region of the calculated dispersion relation may be reliable, the details of these curves should be interpreted with caution.

It is interesting to note that one consequence of the extreme anisotropy of the forces in graphite is the almost quadratic form of the dispersion relation at small q for the $TA_\perp$ branch. For small

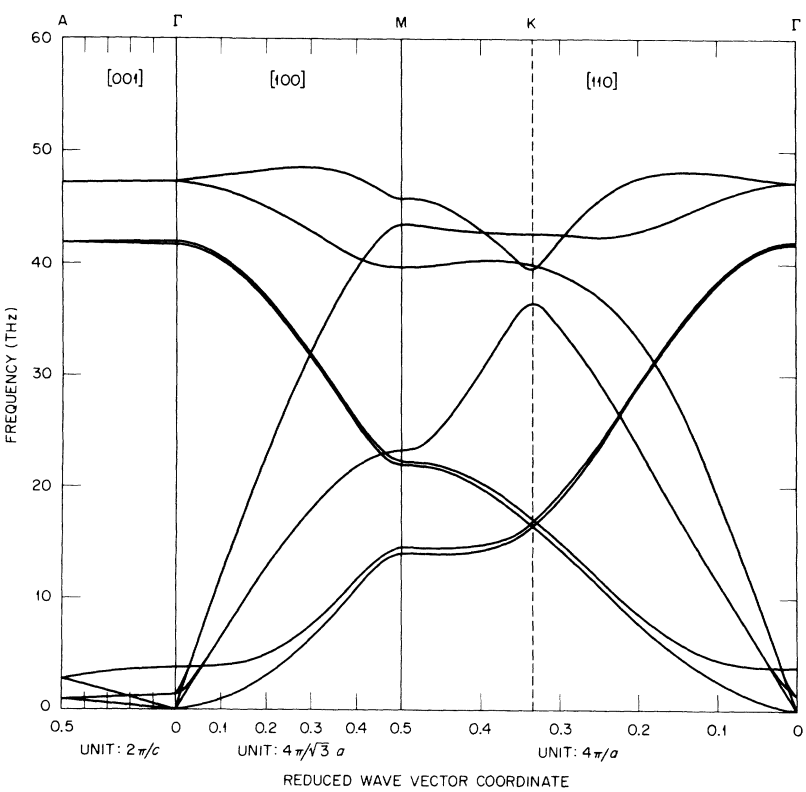

FIG. 8. Phonon dispersion relation for graphite in the [001], [100], and [110] directions as calculated with the fourth-nearest-neighbor AS model discussed in the text.

TABLE III. Elastic constants for graphite (10^{11}dyn/cm^2).

	Calculated from force model[a]	Measured by velocity of sound[b]
C_{11}	144 ± 20	106 ± 2
C_{33}	3.71 ± 0.05	3.65 ± 0.1
C_{44}	0.46 ± 0.02	0.40 ± 0.04
C_{66}	46	44 ± 2

[a]Error estimates based on error of neutron data.
[b]E. S. Seldin.

q, this branch has the form

$$\nu^2 a\ Aq^2 + Bq^4 , \qquad (2)$$

as shown previously by Komatsu[2] using an elasticity theory for graphite which did include a finite C_{44}. At very small q, ν varies linearly with q, as it must because of the term $\sqrt{A}q$. However, the coefficient A, which is proportional to C_{44} and hence proportional to the small constant ϕ_t^4 through the linear combination of the ϕ_t^i's given in Eq. (1), is very much smaller than B which is given by a different linear combination of the very large constants ϕ_t^1, ϕ_t^2, and ϕ_t^3. Thus as q increases, the Bq^4 term soon dominates in Eq. (2) to give $\nu\alpha q^2$. While this qualitative behavior is predicted by Komatsu's theory, the quantitative agreement between his calculations and our measurements is not good because he used values for C_{44} which apparently are not appropriate for the pyrolytic graphite used in this work.

The elastic constants of graphite which are calculated with the AS model are compared to the measurements of Seldin[11] in Table III. The agreement between the two sets of constants is rather good except for C_{11}. This constant gives the initial slope of the LA branch in the [100] direction and in the present work is determined by the data obtained in configuration IV. These data are the most difficult of those obtained in this experiment to interpret reliably, so that the discrepancy may not be unreasonable. However, the excellent agreement obtained between the calculated and measured neutron-intensity distributions, as illustrated in Fig. 5, leads us to suspect that the true value of C_{11} for graphite is probably intermediate between the values given in the table.

The frequency-distribution function $g(\nu)$ was calculated from the AS model using the method described by Raubenheimer and Gilat[8] appropriately modified for the graphite lattice. The results are illustrated in Fig. 9. The general features of this $g(\nu)$ and that calculated by Young and Koppel[4] are very different, although both distributions have pronounced peaks near ~4, ~14, and ~48 THz.

The lattice specific heat at constant volume C_v has been calculated with the $g(\nu)$ obtained in this work. One of the interesting features of the experimental results for C_v is the transition from a T^3 behavior expected for any solid at very low temperatures to an almost T^2 behavior at higher temperatures (10 °K) expected for a two-dimensional lattice. The calculated C_v reproduces almost exactly the observed behavior as illustrated in Fig. 10 where the experimental results for natural graphite,[12] corrected for an electronic contribution using $\gamma = 0.6 \times 10^5$ cal deg^{-2}/mole,[1,12] are also shown.

IV. SUMMARY

The frequencies of certain normal modes of vibration of the graphite lattice have been studied on samples of high-quality pyrolytic graphite by neutron-coherent inelastic-scattering techniques. Some of the data are not compatible with certain

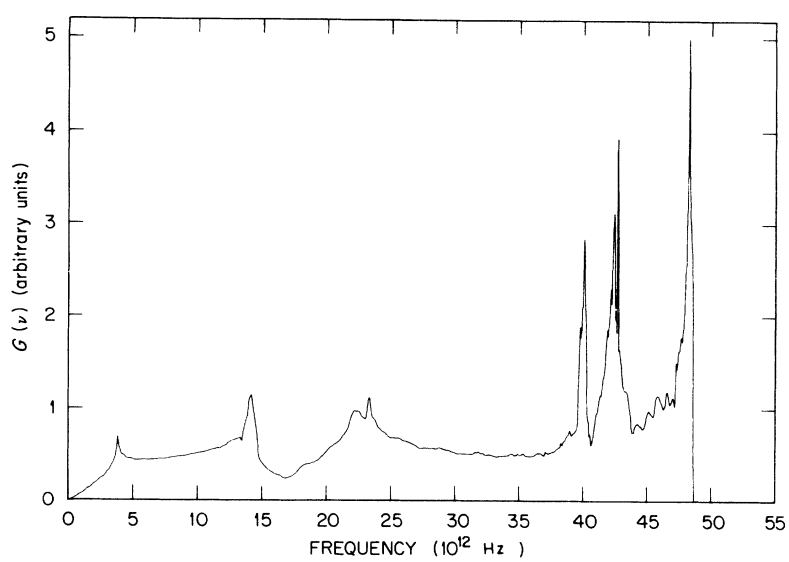

FIG. 9. Frequency-distribution function for graphite calculated with the fourth-nearest-neighbor AS model.

restrictions imposed by the valence-bond model as presented by Young and Koppel.[4] Therefore, the data have been analyzed in terms of a simple axially symmetric Born–von Kármán force-constant model. The results show that appreciable interactions exist between third nearest neighbors in the basal plane. The force model has been used to calculate a frequency-distribution function and the lattice specific heat of graphite. These calculations are in excellent agreement with the specific heat measured for natural graphite in the temperature range 1.5–300 °K.

ACKNOWLEDGMENTS

We are grateful to Dr. C. J. Sparks for his interest in this work and for allowing us to examine the excellent sample he had obtained on loan from the Union Carbide Corp. Laboratory at Parma, Ohio. The valuable technical assistance of J. L. Sellers is also gratefully acknowledged.

APPENDIX

The intensity I observed for a given setting (e.g., ν, $\vec{Q}$) of the neutron spectrometer is given by the convolution of the scattering cross section σ with the resolution function of the spectrometer R centered on (ν, $\vec{Q}$),[13] viz.,

$$I(\nu,\vec{Q}) = \int R(\nu+\Delta\nu, \vec{Q}+\Delta\vec{Q})\,\sigma(\nu+\Delta\nu,\ \vec{Q}+\Delta\vec{Q})\,\Delta\vec{Q}\Delta\nu. \tag{A1}$$

The resolution function can, to a very good approximation, be described by a Gaussian-like function in four dimensions as[13]

$$R(\nu+\Delta\nu,\ \vec{Q}+\Delta\vec{Q}) = R_0 \exp\left(-\tfrac{1}{2}\sum_{k,l=1}^{4} M_{kl} X_k X_l\right), \tag{A2}$$

where $X_1 = \Delta Q_x$, $X_2 = \Delta Q_y$, $X_3 = \Delta Q_z$, and $X_4 = \Delta\nu$. R_0 and M_{kl} are involved functions of such instrumental parameters as the mosaic spreads and d spacings of the monochromator and analyzer crystals, the beam divergencies' $\vec{k}_0$, $\vec{k}'$, etc. For the case of one-phonon scattering by a single crystal it is often sufficient in the evaluation of $I(\nu,\vec{Q})$ merely to replace σ by a δ function, thereby ensuring that only those points ($\nu+\Delta\nu$, $\vec{Q}+\Delta\vec{Q}$) which coincide with the phonon dispersion relation (or surface) are included in the integration. In the present problem, however, for configuration II (and IV) in Fig. 1, we must take into account the orientation randomness of the sample as well as the fact that the cross section depends on the phonon frequency and on the orientation of the phonon polarization vector $\vec{e}$ with respect to $\vec{Q}+\Delta\vec{Q}$. To describe the calculations carried out we will consider the case of $\vec{Q}$ at the 111 ring. It is also convenient to define an orthogonal (xyz) coordinate system with the origin located at $\vec{Q}$, the intersection of the 111 ring and the scattering plane (defined by the vectors $\vec{k}_0$ and $\vec{k}'$ in Fig. 1), and with x parallel to the c axis, y perpendicular to the 111 ring, and z perpendicular to the scattering plane.

For graphite the 111 point corresponds to a Brillouin-zone origin ($\vec{q}=0$) near which the TO $(0,0,\zeta)$ modes would be studied because the structure factor is large for neutron scattering by these modes. In fact with the geometry under discussion, scattering is produced by any optic phonon polarized nearly perpendicular to the c axis and having a wave vector terminating within the limits of the instrumental resolution. The only such modes we need to consider in addition to the TO $(0,0,\zeta)$ mode, are the LO and TO (often called $TO_{\parallel}$) modes, which have wave vectors in or nearly in the basal plane and which are degenerate at $\vec{q}=0$ with the TO $(0,0,\zeta)$ branch. On the basis of our experimental observations, together with various model calculations, it appears that to a good approximation the dispersion surfaces for these modes are quadratic for small wave-vector components in the basal plane. Also, since the dispersion relation for the TO $(0,0,\zeta)$ branch near $\vec{q}=0$ varies slowly with ζ (our x coordinate) the dispersion surface near 111 for the $TO_{\parallel}$ branch can be approximated by $\nu_T = \nu_0 + \alpha_T(y^2+z^2)$, where the dependence on x

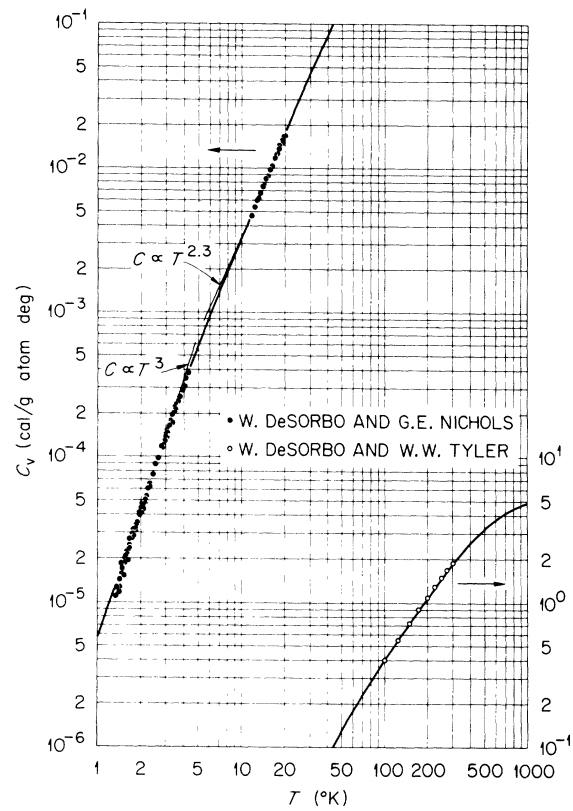

FIG. 10. Comparison of the measured specific heat and that calculated from the frequency distribution function shown in Fig. 9.

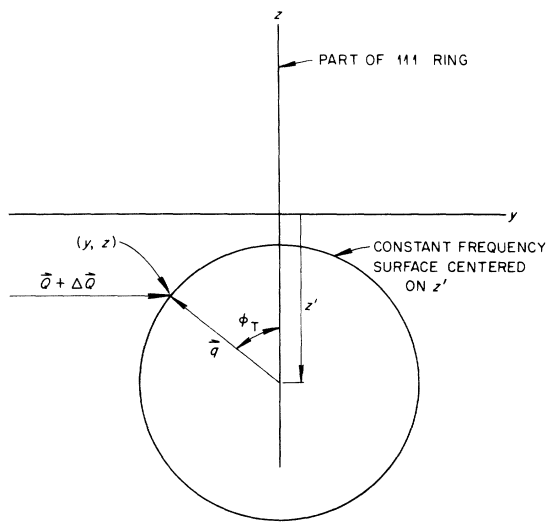

FIG. 11. Schematic diagram illustrating some of the important geometrical factors considered in the calculated intensity vs frequency curve for the TO(00ζ) branch at $\zeta = 0$.

has been neglected, α_T is a constant appropriate to the transverse branch, and ν_0 is the $\vec{q}=0$ frequency. If the position of the center of the resolution function on the frequency axis is denoted ν, then $\Delta\nu_T = \nu_0 - \nu + \alpha_T(y^2+z^2)$. A similar expression holds for the LO branch.

To take into account the orientation randomness of the sample, we assume that any point, for example z', on the z axis is an origin for a dispersion surface. The corresponding expressions for ν_T and $\Delta\nu$ become

$$\nu_T' = \nu_0 + \alpha_T[y^2 + (z'-z)^2] \ ,$$
$$\Delta\nu_T' = \nu_0 - \nu + \alpha_T[y^2 + (z'-z)^2] \ . \qquad \text{(A3)}$$

The intersection of one such surface with the yz plane is illustrated in Fig. 11. There are obviously many such surfaces which pass through the point (y, z), each corresponding to a different z' and hence each having a different ν_T'. In addition, the polarization-dependent part of the cross section, i.e., $[(\vec{Q}+\Delta\vec{Q})\cdot\vec{e}]^2$, which is proportional to $\cos^2\phi$, where ϕ is the angle between $\vec{Q}+\Delta\vec{Q}$ and $\vec{e}$, also obviously depends strongly on z'. For example, for a transverse mode having a wave vector in the yz plane,

$$\cos^2\phi_T = (z'-z)^2/[y^2+(z'-z)^2] \ . \qquad \text{(A4)}$$

We further assume that all modes are purely longitudinal or purely transverse, independent of the orientation of the wave vector $\vec{q}$, and that the dominant influence of $\cos^2\phi$ on the intensity calculation can be retained by ignoring the dependence of $\cos^2\phi$ on x for those wave vectors which are tilted slightly out of the basal plane. The influence of the orientation randomness is therefore accounted for by integrating Eq. (A1) over z'.

After one makes a transformation from the ΔQ_x, ΔQ_y, ΔQ_z coordinates to the xyz coordinates, thereby changing M_{kl} to M_{xy}, the intensity observed when the resolution function is centered on the point $(\nu, \vec{Q})$ can be written formally as

$$I(\nu,\vec{Q}) = \int_{-\infty}^{\infty}[w_T\cos^2\phi_T\, R(x,y,z,\Delta\nu_T') + w_L\cos^2\phi_L R(x,y,z,\Delta\nu_L')]\,dx\,dy\,dz\,dz' \ , \qquad \text{(A5)}$$

where the $\Delta\nu$'s and ϕ's are given by Eqs. (A3) and (A4) and their obvious extensions to the branch having the other polarization. Since we have assumed δ functions for the widths of the dispersion surfaces, the integration over $\Delta\nu$ in Eq. (A1) merely results in a replacement of $\Delta\nu$ in R by the expressions for $\Delta\nu_T'$ (and $\Delta\nu_L'$) given in Eq. (A3). The w's are frequency-dependent weighting factors which have the form

$$w_T = [1 + (e^{h\nu_T'/kT} - 1)^{-1}]/\nu_T' \ .$$

Using the assumptions mentioned above, and noting that the form of the exponents of R excludes the existence of a line in the four-dimensional space $xyz\nu$ along which the exponent remains finite for $xyz \to \infty$, one can carry out the integration over x and z' individually and analytically. With the substitution $s = z' - z$, the only term in the integral that depends explicitly on z' is of the form

$$e^{-M_{zz}(z)^2/2} = e^{-M_{zz}(z'-s)^2/2} .$$

The integral over z' then eliminates M_{zz} from the remaining calculation, which involves the numerical integrations over the variables y and s.

The result of a constant $\vec{Q}$ calculation of I vs ν for the conditions used in this experiment and for $\nu_0 = 1.35$ THz is shown in Fig. 12. The values we

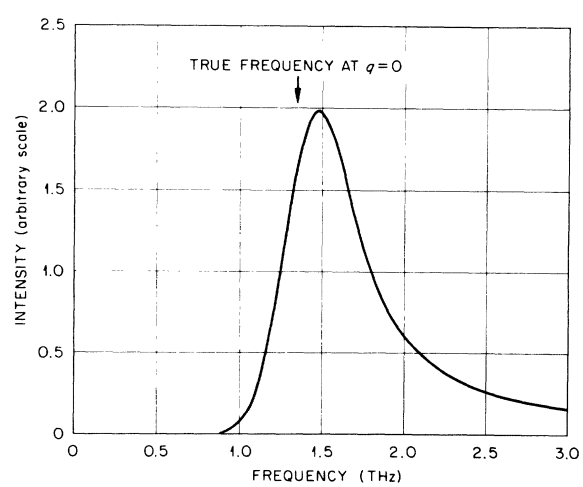

FIG. 12. Calculated intensity distribution for a constant-Q scan of the TO(00ζ) branch for $\zeta = 0$.

used for the constants α_T and α_L were based on the shapes of dispersion surfaces for the ν_T and ν_L branches that were calculated from the force-constant-model fit to our data. The maximum intensity occurs at a frequency higher than ν_0 mainly for two rather obvious reasons. First, even for a single crystal of graphite, the dispersion surfaces for ν_L and ν_T are very steep so that the resolution function samples an appreciable number of modes having frequencies higher than ν_0. Second, because of the orientation randomness, for any frequency ν greater than ν_0 there is a $\nu_T' = \nu$ mode having a wave vector which falls within the resolution (from an origin z') and having a favorable polarization. The long intensity tail at high frequencies is due mainly to the latter effect.

In carrying out this calculation we have fixed the parameters specifying the resolution function at those values which are appropriate for a measurement of $\nu_0 = 1.35$ THz, i.e., we have not taken into account, for example, the dependence of the resolution on $\vec{k}_0$ for $\nu > \nu_0$. Thus the relative intensity calculated for ν appreciably greater than ν_0 is subject to some error. However, the excellent agreement found between the calculated peak shape and the experimental results (see Fig. 2) for ν near ν_0 indicates that this error and those arising from the assumptions mentioned above are probably insignificant for our purposes.

The calculations for the constant-E scans of the LO phonons near the (111) ring were carried out similarly, but with the exception that the intensity was computed for the resolution function centered on differing points along the y axis with ν fixed. These calculations are also in very good agreement with the measurements as shown in Fig. 5.

*Research sponsored by the U. S. Atomic Energy Commission under contract with Union Carbide Corp.

[1]J. A. Krumhansl and H. Brooks, J. Chem. Phys. 21, 1663 (1953); J. C. Bowman and J. A. Krumhansl, J. Phys. Chem. Solids 6, 367 (1958).

[2]K. Komatsu, J. Phys. Soc. Japan 10, 346 (1955); J. Phys. Chem. Solids 6, 381 (1958).

[3]A. Yoshimori and Y. Kitano, J. Phys. Soc. Japan 11, 352 (1956).

[4]James A. Young and Juan U. Koppel, J. Chem. Phys. 42, 357 (1965).

[5]G. Dolling and B. N. Brockhouse, Phys. Rev. 128, 1120 (1962).

[6]J. C. Gylden Houmann and R. M. Nicklow, Phys. Rev. B 1, 3943 (1970).

[7]R. M. Nicklow, N. Wakabayashi, and P. R. Vijayaraghavan, Phys. Rev. B 3, 1229 (1971).

[8]L. J. Raubenheimer and G. Gilat, Phys. Rev. 157, 586 (1967).

[9]J. L. Warren, J. L. Yarnell, G. Dolling, and R. A. Cowley, Phys. Rev. 158, 805 (1967).

[10]F. Fuinstra and J. L. Koenig, Bull. Am. Phys. Soc. 15, 296 (1970).

[11]E. S. Seldin, in *Proceedings of Ninth Biennial Conference on Carbon, Chestnut Hill, Massachusetts*, 1969 (Defense Ceramic Information Center, Columbus, Ohio, 1969) p. 59.

[12]W. DeSorbo and G. E. Nichols, J. Phys. Chem. Solids 6, 352 (1958); W. DeSorbo and W. W. Tyler, General Electric Technical Report No. RL-1202, 1954 (unpublished); see also Ref. 4.

[13]M. J. Cooper and R. Nathans, Acta Cryst. 23, 357 (1967).

PHYSICAL REVIEW B VOLUME 5, NUMBER 12 15 JUNE 1972

Theory of Critical-Fluctuation-Enhanced Raman Scattering by Phonons in NH_4Br

J. B. Sokoloff
Department of Physics, Northeastern University, Boston, Massachusetts 02115
(Received 28 June 1971)

The hypothesis due to Wang and Fleury that the Raman scattering from the 56-cm^{-1} phonon in NH_4Br is enhanced by critical fluctuations in the neighborhood of the transition temperature is derived from a theory of Raman scattering from phonons in a system with partially disordered force constants, by making some reasonable assumptions about the behavior of the polarizability as a function of ammonium-ion orientation.

Ammonium bromide crystallizes in a CsCl structure lattice below 457.7 °K.[1] Since the ammonium ion is of tetrahedral symmetry, it has two possible orientations in its cubic environment. Below a temperature of 235 °K, the ammonium ions in rows parallel to one of the crystallographic axes (let us call it the z axis) order such that all the ions in a given row are oriented the same way and ions in neighboring rows have opposite orientation.[1,2] Wang and Fleury[2] found that above this transition temperature, in addition to a first-order Raman spectrum reflecting the single-phonon density of states because of the breakdown of $\vec{k}$ conservation, there is a fairly well-defined phonon peak